

Attoseconds and the exascale: on laser plasma surface interactions



Robin Timmis
Your College
University of Oxford

A thesis submitted for the degree of
Doctor of Philosophy

Michaelmas 2014

Acknowledgements

Personal Institutional

The author thanks the Norreys Research Group, Prof. Philip Burrows and Dr. Qingsong Feng for useful discussions, the SMILEI consortium and the ARCHER2 support team. The authors also acknowledge the support of AWE plc, UKRI-EPSRC and the Oxford-Berman Graduate Scholarship program. This work used the ARCHER2 UK National Supercomputing Service (<https://www.archer2.ac.uk>) under project e674 of URKI-EPSRC grant no. EP/R029148/1 and UKRI-STFC grant no. ST/V001655/1.

Abstract

The commissioning of multi-petawatt class laser facilities around the world is gathering pace. One of the primary motivations for these investments is the acceleration of high-quality, low-emittance electron bunches. Here we explore the interaction of a high-intensity femtosecond laser pulse with a mass-limited dense target to produce MeV attosecond electron bunches in transmission and confirm with three-dimensional simulation that such bunches have low emittance and nano-Coulomb charge. We then perform a large parameter scan from non-relativistic laser intensities to the laser-QED regime and from the critical plasma density to beyond solid density to demonstrate that the electron bunch energies and the laser pulse energy absorption into the plasma can be quantitatively described via the Zero Vector Potential mechanism. These results have wide-ranging implications for future particle accelerator science and associated technologies.

Contents

List of Figures	ix
A List of Symbols and Abbreviations	xi
1 Attosecond X-ray harmonics on the ORION laser facility	1
1.1 A plan	1
1.2 The experiment	2
1.3 Theory	2
1.3.1 The ROM model	2
1.3.2 The normalisation factor	3
1.3.3 Hole boring	4
1.3.4 Harmonic source size	8
1.4 Simulations	8
1.4.1 1D PIC simulations of HHG	8
1.4.2 Hydrodynamic simulations of preplasma formation	14
1.5 Experimental data processing	14
1.5.1 Image plate calibration	14
1.5.2 OHREX calibration	16
1.5.3 Extracting the data	18
Appendices	
References	25

List of Figures

1.1	2D PIC simulation of HHG beaming effect via hole boring.	5
1.2	Typical 1D HHG Smilei simulation results	9
1.3	Comparison between simulation and analytical predictions of hole boring and HHG normalisation factor.	11
1.4	The effect of the PIC code particle shape function on numerical heating. .	12
1.5	Reflected beam harmonic content up to the keV range in a high resolution 1D PIC simulation.	13
1.6	Attosecond pulse train from the filtered reflected laser pulse.	14
1.7	Unprocessed IP from ORION experiment	19
1.8	Typical ORION experiment uncalibrated IP response quartz (10 $\bar{1}$ 0) crystal and Fourier transform	20
1.9	Typical ORION experiment calibrated IP response for the quartz (10 $\bar{1}$ 1) crystal.	21

x

A List of Symbols and Abbreviations

Note All quantities are defined in SI units unless otherwise specified throughout the thesis.

α	Twiss parameter = $-\frac{\langle x_i x'_i \rangle}{\epsilon_{\text{rms}}^i}$
a_0	Normalised vector potential = $\frac{e \mathbf{E}_L }{m_e c \omega_L}$
A	Atomic mass number
\mathbf{A}	Three-vector potential
\mathbf{A}^μ	Four-vector potential = $(\phi/c, \mathbf{A})$
β	Normalised speed = v/c or Twiss parameter = $\frac{\langle x_i \rangle}{\epsilon_{\text{rms}}^i}$
β	Normalised velocity = \mathbf{v}/c
\mathbf{B}	Magnetic field
\mathbf{B}_L	Magnetic field of a laser pulse
c	Speed of light = $3.00 \times 10^8 \text{ m s}^{-1}$
δ	Skin depth
$\delta(\mathbf{x})$	Dirac-delta function
$d\mathbf{s}$	Vector line element
Δ	Change in a variable
D	Number of dimensions
∇	Partial derivative = $\hat{\mathbf{x}}_\mu \frac{\partial}{\partial x_\mu}$, $\mu = x, y, z$
ϵ_0	Permittivity of free space = $8.854 \times 10^{-12} \text{ F m}^{-1}$
ϵ_{rms}	Transverse geometric emittance
$\epsilon_{n,\text{rms}}$	Transverse normalised emittance
e	Absolute charge of an electron = $1.602 \times 10^{-19} \text{ C}$
e^\pm	Electron (−) or positron (+)
\mathbf{E}	Electric field
E_S	Schwinger electric field = $1.3 \times 10^{18} \text{ V m}^{-1}$

E _L	Electric field of a laser pulse
<i>f</i>	Distribution function
F _L	Lorentz force = $q(\mathbf{E} + \mathbf{v} \times \mathbf{B})$
γ	Lorentz/gamma factor = $\frac{1}{\sqrt{1-\beta^2}}$ or Twiss parameter = $\frac{\langle x_i'^2 \rangle}{\epsilon_{\text{rms}}^i}$ or high-energy photon
η	Efficiency
<i>I</i>	Electromagnetic field intensity
\mathcal{H}	Hamiltonian
θ	Angle of incidence of a laser pulse
J	Current density
k	Electromagnetic three-wave vector
K ^{μ}	Electromagnetic four-wave vector = $(\omega/c\mathbf{k})$
<i>K</i>	Boltzmann constant = $1.38 \times 10^{-23} \text{ J K}^{-1}$
λ_D	Debye length $\equiv \sqrt{\frac{\epsilon_0 K T_e}{n_e e^2}}$
λ_L	Laser pulse wavelength
Λ_ν^μ	Lorentz transformation matrix
<i>L</i>	Length
\mathcal{L}	Lagrangian
μ_0	Vacuum permeability = $1.257 \times 10^{-6} \text{ N A}^{-2}$
<i>m</i> _e	Mass of an electron = $9.11 \times 10^{-31} \text{ kg}$
<i>n</i>	Harmonic order
<i>n</i> , <i>N</i>	Number
<i>n</i> _c	Plasma critical density = $\frac{\omega_L^2 m_e \epsilon_0}{e^2}$
<i>n</i> _e	Plasma electron number density
\bar{n}_e	Normalised plasma electron number density = $\frac{n_e}{n_c}$
<i>n</i> _i	Plasma ion number density
n	Vector normal to a surface
<i>N</i> _A	Avogadro's number
<i>N</i> _D	Number of particles within the Debye sphere = $\frac{4}{3}\pi\lambda_D^3 n$
ω	Angular frequency of an oscillation or low energy photon
ω_L	Laser pulse angular frequency

ω_p	Plasma frequency = $\sqrt{\frac{e^2 n_e}{m_e \epsilon_0}}$
ϕ	Angle of laser polarisation out of the plane of interaction or scalar electromagnetic potential
\mathbf{p}	Three-momentum
P	Pressure
\mathbf{P}^μ	Four-momentum = $(U/c, \mathbf{p})$
Q	Charge
ρ	Density
r_L	Relativistic Larmor radius = $\frac{\gamma m_e v}{e \mathbf{B} }$
\mathbf{r}	Radial vector
$\hat{\mathbf{r}}$	Radial unit vector
R	Rate
σ	Surface area
S	Relativistic similarity parameter = \bar{n}_e/a_0
$S(\mathbf{x})$	Shape function
τ	Average time or standard deviation of time
t	Time
T	Kinetic energy
T_e	Plasma electron temperature
u, v	Speed
\mathbf{u}, \mathbf{v}	Velocity
U	Energy
v_ϕ	Phase velocity
V	Potential or volume
w_L	Beam waist
w_p	Quasi-particle weight
χ_γ	Photon quantum parameter
x, y, z	Standard Cartesian coordinates in 3D
$\mathbf{x}, \mathbf{y}, \mathbf{z}$	Vectors along each axis of the Cartesian coordinate system
$\hat{\mathbf{x}}, \hat{\mathbf{y}}, \hat{\mathbf{z}}$	Unit vectors along each axis of the Cartesian coordinate system
Z	Ion charge state in units of e

Subscripts . . .	The following are defined the subscripts
C	Pseudocapacitor
e	Electron
γ	Photon
L	Laser pulse or Longitudinal
T	Transvere to a laser pulse
pol	Along the polarisation vector of a laser pulse
\perp	Perpendicular
\parallel	Parallel
i, j	Indices
s	Species
x, y, z	Along the specific Cartesian axes
∞	
The hat symbol	To represent a normalised vecotr
primed coordinates	and reference frames
1D, 2D, 3D . .	One-, two- or three-dimension(al)
BW	Breit-Wheeler
CLF	Central Laser Facility
CPA	Chirped Pulse Amplification
CSE	Coherent Synchrotron Emission
FDTD	Finite Difference Time Domain
HB	Hole Boring
HED	High-Energy-Density
HHG	High Harmonic Generation
HPC	High Performance Computing
OHREX	ORION High Resolution X-ray
PIC	Particle-In-Cell
QED	Quantum Electro-Dynamics
ROM	Relativistic Oscillating Mirror
RPM	Relativistic Plasma Mirror
RR	Radiation Reaction
SF-QED	Strong-Field Quantum Electro-Dynamics
ZVP	Zero Vector Potential

1

Attosecond X-ray harmonics on the ORION laser facility

Contents

1.1	A plan	1
1.2	The experiment	2
1.3	Theory	2
1.3.1	The ROM model	2
1.3.2	The normalisation factor	3
1.3.3	Hole boring	4
1.3.4	Harmonic source size	8
1.4	Simulations	8
1.4.1	1D PIC simulations of HHG	8
1.4.2	Hydrodynamic simulations of preplasma formation	14
1.5	Experimental data processing	14
1.5.1	Image plate calibration	14
1.5.2	OHREX calibration	16
1.5.3	Extracting the data	18

1.1 A plan

This chapter reports on the March 2023 experiment at the ORION laser facility, AWE, Aldermaston. The UK's most powerful sub-picosecond laser.

Important sections include: HYADES scale length sims, ORION parameters and

description of the setup, targets etc, data analysis after, beamlet sims, HHG theory

I think the appropriate order would be theory, simulation, experiment layout, data analysis since then I can use all things inferred from theory and simulation to justify the data analysis. It also means ending well.

The early developments in the field are outlined by Teubner *et al* [1].

HHG from solids has demonstrated significantly higher conversion efficiencies than for HHG from gases nor are there any limitations to the applied laser intensity [1]. SHHG has thus been a field of huge interest over the past three decades for the production of bright coherent attosecond harmonics.

1.2 The experiment

The experiment goal was

The ORION target chamber

Details and layout

1.3 Theory

1.3.1 The ROM model

Apply Bourdier method and conservation of generalised momentum, we see that

and thus non-linearity

and thus the thing we need to solve is blah.

The laser pulse leads to macroscopic oscillation of the plasma surface and therefore a corresponding oscillation of the ARP. One can understand this leading to a sub cycle Doppler shift in the reflected pulse. These pulses of radiation separated by the laser pulse frequency must therefore in the spectral domain consist of HH.

The Relativistic Oscillating Mirror (ROM) model describes an extension.

The following outlines the key ideas

Ok: assume I have the expression from Baeva's paper (do this tomorrow)

1.3.2 The normalisation factor

Baeva's theory provides us with the relative intensity of harmonics. However, for comparison with the absolute spectral intensity of harmonics in experiment, the normalisation factor is required. This can be calculated from conservation of energy. For arbitrary harmonic order scaling, n^{-p} , the spectral intensity of the harmonic beam is

$$I_\omega(\omega) = \frac{dE_\omega(J)}{dAd\omega} = I_0 \sum_{n=1, \text{ odd}}^{n_C} n^{-p} S_n \left(\frac{\omega}{\omega_L} - n \right) \quad (1.1)$$

up to the cutoff, n_C . Here $S_n(\omega/\omega_L - n)$ is the spectral shape function of the n^{th} harmonic in reciprocal space and I_0 is the normalisation factor of interest. From conservation of energy,

$$\int I_\omega(\omega) d\omega dA = ER, \quad (1.2)$$

where E the total energy of the laser pulse and R is the reflectivity of the Relativistic Plasma Mirror (RPM). Intuition suggests the spectral shape function for the n^{th} harmonic retains the spectral shape of the incident laser pulse, *i.e.* for a laser pulse with a Gaussian temporal profile, this corresponds to a Gaussian centred at $n\omega_L$ of width $\sigma_L = 1/t_L$, where t_L is the laser pulse width. Simulations show this is a reasonable approximation for ORION parameters ¹.

Simulations also show that for the SP1 laser, the incident laser pulse significantly suppresses the even harmonics, hence,

$$ER = \int_0^\infty I_0 \sum_{n=1, \text{ odd}}^{n_C} n^{-p} e^{-(\omega/\omega_L - n)^2/\sigma_L^2} d\omega. \quad (1.3)$$

The integral and summation order can be reversed. Since $\sigma_L \ll \omega_L$, all integrals in the summation are $\approx \int_{-\infty}^\infty$ and therefore,

$$ER \approx I_0 \sum_{m=0}^{n_C/2-1} (1+2m)^{-p} \sqrt{\pi} \sigma_L \omega_L, \quad (1.4)$$

¹Hole boring discussed in the following section can lead to a Doppler shift in harmonic energy across the laser pulse corresponding to a Doppler broadening of the spectral shape function in reciprocal space, however, unlike the ZVP simulations of the previous chapter, this is negligible for ORION parameters.

thus,

$$ER \approx I_0 \sqrt{\pi} \sigma_L \omega_L ((1 - 2^{-p}) \zeta(p) - 2^{-p} \zeta(p, \frac{n_C + 1}{2})), \quad (1.5)$$

where $\zeta(p)$ and $\zeta(p, (n_C + 1)/2)$ are the Riemann Zeta and Hurwitz Zeta functions respectively. The final term can be neglected for a petawatt class laser pulse where $n_C \gg 1$. In the case of an ideal p -polarised laser pulse,

$$ER \approx I_0 \sqrt{\pi} \sigma_L \omega_L \zeta(p). \quad (1.6)$$

For the ROM regime, $p = 8/3$ and the RPM is extremely efficient, $R \approx 1$. Thus, I_0 can be estimated from the system parameters.

1.3.3 Hole boring

As observed in the ZVP plots, on long timescales relative to the laser pulse cycles, via the ponderomotive pressure of the laser, the plasma front moves inwards. This is hole boring [2]. One can derive a hole boring velocity by considering conservation of momentum in this quasi-static state. Since the hole boring velocity is laser pulse intensity dependent, the spatial profile of the laser will be imprinted on the surface. Typically Gaussian in shape, for high power laser systems, this can to first order generate a focusing RPM and a beaming of the specularly reflected signal, as in Figure 1.1. To access the highest possible electromagnetic field intensities, the laser pulse is focused on target to the diffraction limit. However, since the diffraction limit scales linearly with the wavelength, higher-order harmonics can be refocused to a smaller spot via this mechanism allowing access to unprecedented peak intensities. Vincenti *et al* demonstrated intensity gains of over 1000 with currently accessible parameters in three-dimensions (3D) Particle-In-Cell (PIC) simulations [3], suggesting a realistic route to the Schwinger Limit using next-generation laser facilities. Regardless of any blue-skies purposes, it is clear any prediction of High Harmonic Generation (HHG) beam intensity must account for hole boring and is therefore an essential component of the ORION experiment analysis.

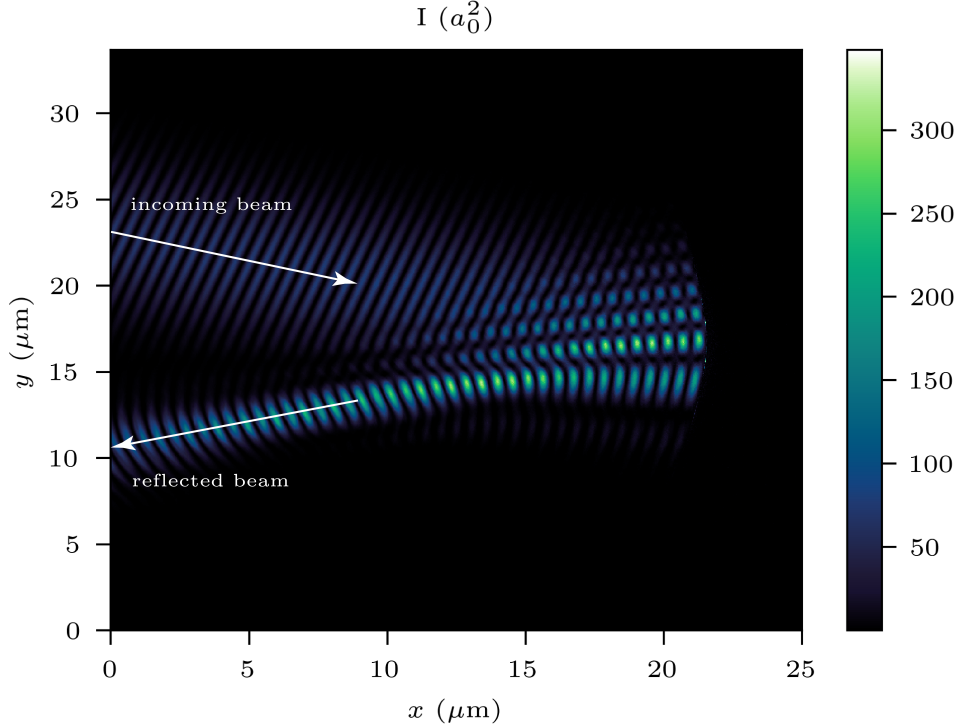


Figure 1.1: Electromagnetic field intensity in a 2D PIC simulation of a relativistic ($a_0 = 30$) laser pulse incident on a solid density plasma. The incoming beam is specularly reflected off the target which is curved by the radiation pressure leading to beaming in the reflected harmonic beam.

Applying momentum balance between the laser pulse and particles in the rest frame of the RPM surface, the hole boring velocity is

$$\frac{v_{\text{HB}}}{c} = \sqrt{\frac{R \cos \theta}{2} \frac{Z m_e}{A m_p} \frac{n_c}{n_e(x_i(t, y))}} a_L(t, y) = \Pi a_L(t, y), \quad (1.7)$$

where R is the RPM reflectivity, θ is the angle of incidence, 16° in the ORION experiment, Z and A are the atomic and atomic mass numbers respectively for the plasma ions, n_c is the plasma critical density, $n_e(x_i(t, y))$ the electron number density and $x_i(t, y)$ the depth of hole boring, from the Supplementary Material [4]. For the ORION laser pulse parameter space $\Pi \ll a_L \forall t$, *i.e.* we are in the relativistic electron and non-relativistic ion regime. Hence, the relativistic correction derived by Robinson *et al* [5] to Equation 1.7 can be neglected. Due to the high contrast and long duration of the ORION beamlines, there is minimal pre-plasma formation on the front surface and therefore the number density is simply the number density

of the material in solid form and n_e is independent of $x_i(t, y)$. Robinson *et al* [6] generalised momentum conservation to multiple species, simply replace the mass density with the composite mass density $\rho = \sum_j m_{ij}n_{ij}$, then

$$\frac{An_e}{Z} \rightarrow \sum_j \frac{A_j n_{ej}}{Z_j}, \quad (1.8)$$

where n_{ej} is the number density of electrons that originated from the j ion.

The spatio-temporal envelope of the normalised vector potential of the laser pulse incident on the target surface is modelled as

$$a_L(t, y) = a_0 e^{-\frac{y^2}{2w_L^2}} g(t - t_0) \quad (1.9)$$

where w_L is the beam waist on target and $g(t)$ the temporal envelope, a Gaussian or sech profile and t_0 the main pulse peak time.

Integrating Equation 1.7,

$$x_i(y) = \int v_{HB} dt = \Pi \int_{-\infty}^t a_L(t, y) c dt. \quad (1.10)$$

At the peak of the main pulse,

$$x_i(y) = \Pi a_0 c e^{-\frac{y^2}{2w_L^2}} G, \quad (1.11)$$

where $G = \int_{-\infty}^{t_0} g(t - t_0) dt \sim t_L$ and t_L is the laser pulse temporal width.

The total denting is a combination of the peak electron-ion charge separation, x_e (which leads to the intrinsic phase of the HHG beam [**anderbruggePropagationRelativisticSurface2**]) and Equation 1.10. Note that for the long pulse duration of the ORION laser, $x_i \gg x_e$ and therefore x_e can be neglected.

Applying a Taylor expansion to the spatial profile of Equation 1.10 around the laser spot centre,

$$x_i = \text{constant} - \frac{y^2}{4f_p} + \mathcal{O}(y^4), \quad (1.12)$$

where, to first order, this is the equation of a parabolic mirror with focal length

$$f_p(t) = \frac{w_L^2}{4\Pi a_0 c G}. \quad (1.13)$$

Following the Vincenti *et al* derivation [4], the denting parameter is defined as,

$$\delta_T = x_i|_{(y=0)} - x_i|_{(y=\sqrt{2}\omega_L)}. \quad (1.14)$$

Hence,

$$\delta_T = \frac{w_L^2}{2f_p} = 2\pi a_0 c G, \quad (1.15)$$

and is independent of laser focal spot size.

If the spatial profile of the n^{th} harmonic beam can be adequately described by a Gaussian at the plasma mirror plane, with a beam width described by the harmonic source size, w_n ,

$$h_n \sim e^{-r^2/w_n^2}, \quad (1.16)$$

then the beam profile is known at all distances, z from the target. Its divergence, defined as

$$\theta_n = \lim_{z \rightarrow \infty} \frac{w_n(z)}{z}, \quad (1.17)$$

is therefore

$$\theta_n = \theta_n^0 \sqrt{1 + \Psi_n^2}, \quad (1.18)$$

where $\theta_n^0 = \lambda_n / \pi w_n$ is the harmonic divergence in the absence of RPM denting and

$$\Psi_n = \frac{2\pi}{\cos \theta} \left(\frac{w_n(0)}{w_L} \right)^2 \frac{\delta_T}{\lambda_n} \quad (1.19)$$

is the dimensionless focusing parameter. If $\Psi_n \gg 1$, as is true for the short wavelength X-ray harmonics of interest,

$$\theta_n \approx \frac{w_n(0)}{f_p \cos \theta} \quad (1.20)$$

and the divergence is dominated by RPM curvature.

Far from focus, at the detector plane $z = 2.4$ m from the target,

$$w_n \approx z \tan \theta_n. \quad (1.21)$$

The corresponding magnification factor at detection is thus

$$\gamma_n(z) = \frac{w_n(z)}{w_n(0)}, \quad (1.22)$$

thus the laser intensity at detection is reduced by a factor $\gamma_n(z)^{-2}$.

At large distances,

$$\gamma_n \approx \frac{z \tan(w_n(0)/(f_p \cos \theta))}{w_n(0))} \quad (1.23)$$

Taking the Taylor expansion of the tangent, one sees that the magnification factor is only weakly dependent on the harmonic source size (f_p is independent of the source size), whereas the magnification is strongly dependent on the the laser spot size ($\sim w_L^4$).

At the new RPM focal point, $z = z_f$, the demagnification factor is [4]

$$\gamma_n(z_f) = \frac{1}{\sqrt{1 + \Psi_n^2}}, \quad (1.24)$$

this determines the new peak intensity accessible via hole boring.

1.3.4 Harmonic source size

Include plots and fits for near roll off.

1.4 Simulations

1.4.1 1D PIC simulations of HHG

Numerical simulations of the SP1 and SP2 interactions with CVD and PMMA were performed using the Smilei PIC code to confirm the results of the previous section for ORION beamline parameters. Application of the Bourdier method (plasma initialised streaming at $\mathbf{v} = c \sin \theta \hat{\mathbf{y}}$) enabled the accurate and computationally efficient reconstruction of the interactions in 1D, a necessity for the sub-ps ORION laser pulse duration. Despite the 1D geometry and optimised supercomputer architecture, resolution numerical heating and noise remained a serious issue. Edwards and Mikhailova noted for their single laser pulse cycle simulations that the highest resolved harmonic required 10 cells per wavelength and up to 5000 particles

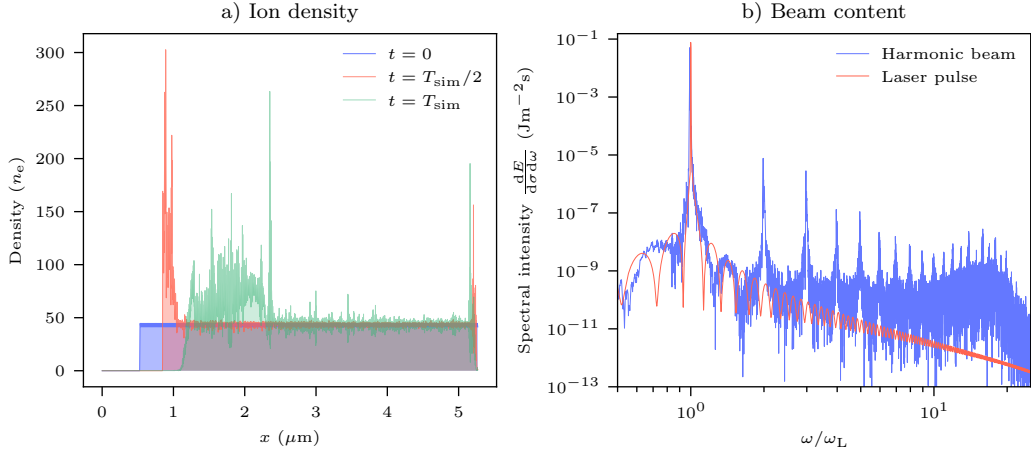


Figure 1.2: 1D PIC simulation of the SP1 ORION beamline geometry at $a_0 = 7$ interacting with a pre-ionised CVD target. a) Ion density at initialisation ($t = 0$), halfway ($t = T_{\text{sim}}/2$) and at the simulation end ($t = T_{\text{sim}}$) demonstrating hole boring. b) Absolute spectral intensity of the laser pulse and reflected harmonic beam obtained via Fourier transforms. The harmonic beam retains the laser pulse spectral width. Even harmonics are significantly suppressed at this polarisation. The large bump in the distribution around the 18th harmonic is spuriously generated via numerical heating.

per cell was necessary for their noise requirements [7] while numerical heating scales linearly with time. The fourth interpolation order for the particle shape function was found to be an efficient choice for the minimisation of numerical heating.

Fortunately, to make comparisons to the derivations of Section 1.3 only a low resolution is necessary. Simulation parameters are detailed in Table 1.1. Parameters are given in real units in the laboratory frame and normalised Smilei units in the boosted Bourdier frame. Note that polarisation angles and normalised vector potentials are unchanged by the frame transformation.

Figure 1.2 presents typical simulation results for the SP1 laser geometry, SP2 simulations produced similar results. Figure 1.2a illustrates how the ion density profile evolves via hole boring. While the density increases to several times its initial level near the plasma surface, this need not be accounted for in the hole boring calculation since these additional ions have already acquired the necessary momentum and are simply propagating inwards with the surface. Figure 1.2b clearly shows the harmonic content of the specularly reflected beam with harmonics retaining the spectral shape of the incident beam. Even harmonics are significantly

SP1 Laser (1D, 16° angle of incidence)		
Parameters	Real	Smilei
Wavelength, λ (nm)	527	2π
Angular frequency, ω_L (fs $^{-1}$)	3.58	1
Polarisation, ϕ (°)	-42.2	-42.2
Normalised vector potential, a_0	7 - 10	7 - 10
Temporal FWHM, t_{FW} (fs)	470	1690
Temporal envelope, E_t	$E_t \sim e^{-(t-t_{FW})^2 \ln 2/t_{FW}^2}$	
SP2 Laser (1D, 16° angle of incidence)		
Wavelength, λ (nm)	1053	2π
Angular frequency, ω_L (fs $^{-1}$)	1.79	1
Polarisation, ϕ (°)	19.6	19.6
Normalised vector potential, a_0	20 - 30	20 - 30
Temporal FWHM, t_{FW} (fs)	470	843
Temporal envelope, E_t	$E_t \sim e^{-(t-t_{FW})^2 \ln 2/t_{FW}^2}$	
Simulation box		
Size, x (nm)	10λ	20π
Sim length, T_{sim} (fs)	$2t_{FW} + 5\lambda/c$	
Spatial resolution, Δx (nm)	$\lambda/128$	
Temporal resolution, Δt (as)	$\Delta x/2c$	
Macro-electrons per cell	1000	
Macro-ions per cell	1000	
Ion temperature, T_i (keV)	0	0
Electron temperature, T_e (keV)	0.115	2.25×10^{-4}
Collisionless, pre-ionised, randomly-initialised plasma		
CVD density, n_e (m $^{-3}$)	1.05×10^{24}	$\begin{cases} 294 & \text{for SP1} \\ 1175 & \text{for SP2} \end{cases}$
PMMA density, n_e (m $^{-3}$)	3.90×10^{23}	$\begin{cases} 109 & \text{for SP1} \\ 435 & \text{for SP2} \end{cases}$
Electron x profile, $n(x)$	n_e for $\lambda \leq x \leq 9\lambda$	

Table 1.1: Smilei parameters to compare Section 1.3 analytical results to numerical simulation for ORION parameter space. Real parameters are taken in the laboratory frame with the given units, while Smilei parameters are in the boosted frame with normalised units. The CVD ion distribution consists of carbon ions with number density $n/6$ while the PMMA ion distribution consists of carbon, oxygen and hydrogen ions with number density $n/6$ respectively, each with 1000 macroparticles per cell.

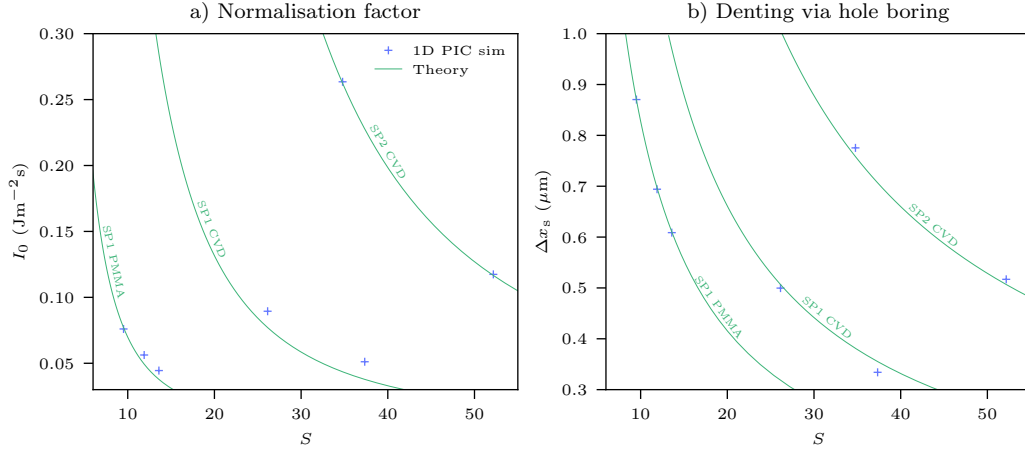


Figure 1.3: Comparison between simulation and analytical predictions of hole boring and HHG normalisation factor in the ORION laser facility parameter space for CVD and PMMA targets. a) The normalisation factor, I_0 , where the spectral intensity, $I = I_0 n^{-p}$ for low order harmonics. b) The depth of hole boring compared to the initialised plasma surface. Note that the steep density gradient as visible in Figure 1.2a ensures the surface position is well defined. Both parameters are expressed in the laboratory frame.

supressed relative to odd harmonics. The bump in the distribution around the 18th harmonic is an entirely numerical effect, increasing the simulation resolution shifts the bump to the right. These simulations had a resolution of 128 cells per laser wavelength, following Edwards and Mikhailova one can only trust this distribution up to the 12th harmonic, at which point the distribution begins to change its shape. Clearly energy conservation does not hold for this simulation, however it is still possible to extract I_0 if we make the reasonable assumption that Debye heating does not affect the HHG process and that the spectrum is simply the sum of the two contributions (justified by the observation of the continuation of harmonics over the bump in the distribution). Thus, I_0 can simply be extracted as the peak intensity of the distribution corresponding to the intensity at $\omega/\omega_L = 1$).

Figure 1.3 compares the analytically calculated parameters with those extracted from the simulations demonstrating excellent agreement for the parameter space accessible with the ORION laser facility and for the assumptions made in the analysis. The effect of numerical heating on the hole boring extent is evident in Figure X where the change in the surface position is plotted over time for the analytical calculation

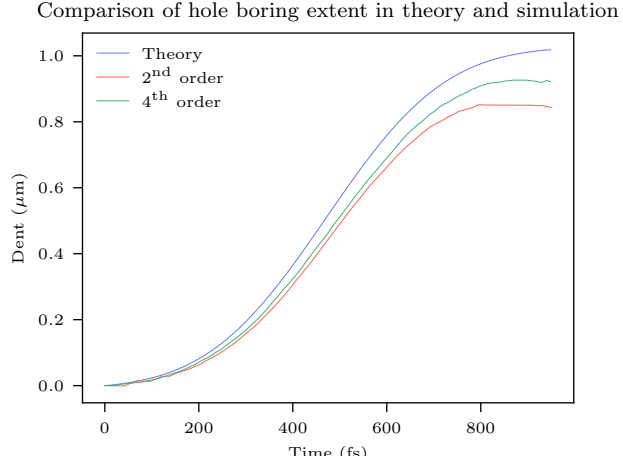


Figure 1.4: The effect of the PIC code particle shape function on numerical heating demonstrated via the extent of hole boring. The deviation from the theoretical prediction increases with time, the error decreases for increasing order of the shape function.

and PIC simulations with 2nd and 4th order shape function. The deviation from the theoretical prediction increases with time. Numerical heating leads to higher electron temperatures at the plasma surface and correspondingly a spurious preplasma expansion analogous to the prepulse preplasma expansion. This is why artificially increasing the plasma temperature to increase the Debye length and reduce numerical heating, while improving HHG accuracy, reduces hole boring accuracy since on sub-ps timescales, there is the potential for significant preplasma expansion.

The X-ray harmonic spectrum produced from a CVD target irradiated by an SP1 type laser pulse is resolved in Figure 1.5. The simulation has 16384 cells per laser wavelength, the minimum multiple of 2 required to resolve the harmonics accessed with the OHREX quartz crystals. It was necessary to use a short test laser pulse with a $5\lambda_L$ FWHM. The simulation time before the peak of laser pulse was increased to reduce the error in the spectrum from unphysical hard cutoffs to the laser pulse profile. A steep preplasma scale length was applied to the plasma distribution of $0.04\lambda_L$ to model the peak of the ORION pulse and suppress **CWE!** (**CWE!**). At the X-ray intensities of Figure 1.5b, no harmonic structure is visible, indeed for the non-optimal ORION target chamber geometry, harmonics begin to merge from around the 20th. Note the s-polarised part of the reflected beam is over 50

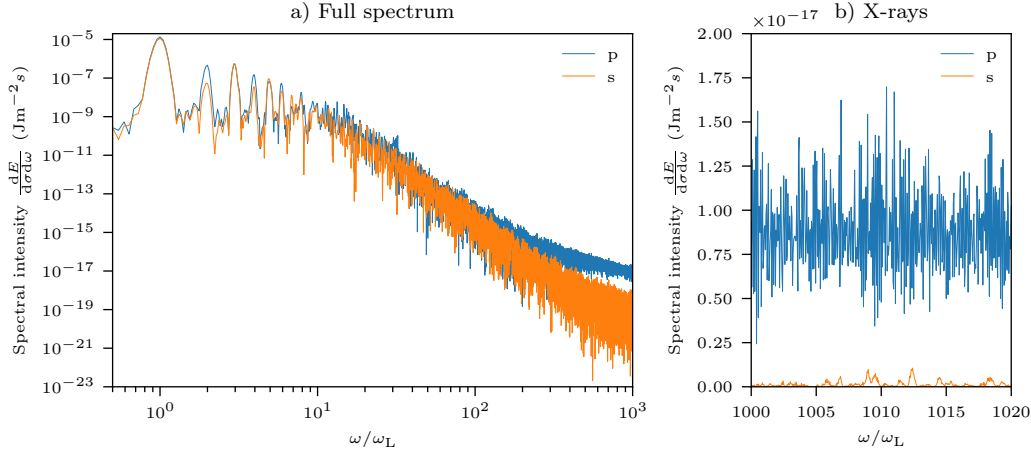


Figure 1.5: Reflected beam harmonic content up to the keV range in a high resolution 1D PIC simulation of a test pulse with SP1 ORION beam geometry incident on a CVD target. The absolute spectral intensity is calculated from the Fourier transform of the reflected beam electric field. The s- and p-polarised components of the beam are analysed separately for both a) the full spectrum and b) the X-ray harmonics accessible with the OHREX quartz ($10\bar{1}1$) crystal.

times weaker than the p-polarised beam at the 1000th harmonic. It would be interesting to extract the reflected beam temporal profile after filtering of sub X-ray harmonics. This can be achieved by applying the inverse Fourier transform to the Fourier transformed temporal profile with the lower order harmonics removed. Unfortunately, beyond $n = 50$, the contribution in the signal from noise prevented the structure from being observed. Figure 1.6 compares the reflected pulse structure to the reflected pulse structure with harmonics below $n = 50$ removed. The filtered beam consists of a series of attosecond pulses of radiation, the brightest pulse is of duration 30.3 as. Note that the intensity of the first few laser cycles is insufficient for the generation of harmonics above $n = 50$ and there is therefore no signal here, reducing the pulse train length.

Beamlet sim

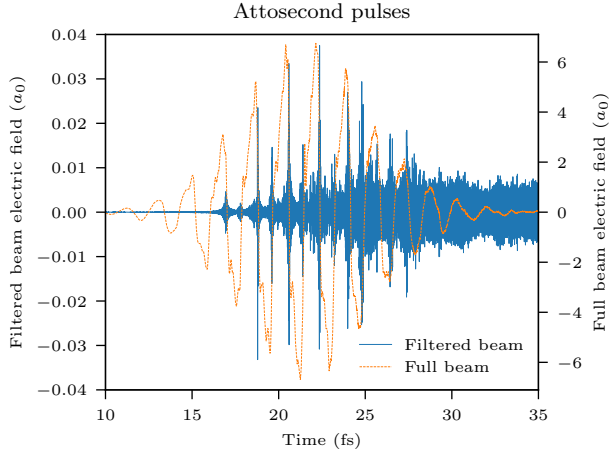


Figure 1.6: Attosecond pulse train from the filtered reflected laser pulse. The filtered beam contains only harmonics above $n = 50$.

1.4.2 Hydrodynamic simulations of preplasma formation

1.5 Experimental data processing

1.5.1 Image plate calibration

Image plates (IPs) are reusable recording media that detect ionising radiation and are particularly suitable for the detection of X-rays produced in laser-plasma interactions. Their response is well understood and their sensitivities to a wide spectrum photon energies have been absolutely calibrated on the ORION facility [8]. Albeit for the FLA3000 scanner not the FLA7000 used in this experiment. However, the deviation in response is negligible for the photon energies measured. In this experiment the Fuji Biological Analysis System (BAS) TR-type IPs were used. They have a phosphor layer composed of $\text{BaFBr}_{0.085}\text{I}_{0.15}$ with density 2.61 g cm^{-3} and thickness $60 \mu\text{m}$ but no mylar layer. This makes them suitable for low energy X-ray detection. When scanned, the IP releases blue photons via photostimulated luminescence (PSL), which is then collected by a photomultiplier tube. The PSL value is generalised across scanner types from the measured ‘Grey’ (G) value by

$$\text{PSL} = (0.23284G^2 \times 10^{-9}) \left(\frac{\Delta x}{100} \right)^2 W \times 10^{-L/2}, \quad (1.25)$$

where Δx is the scanner resolution ($= 25 \mu\text{m}$ in this experiment), L is the latitude parameter, and

$$W = 0.092906 + 1370.8e^{-0.014874V} + 654.24e^{-0.011026}, \quad (1.26)$$

where V is the scanner voltage [9].

IP photon sensitivity, ψ , the number of PSLs per incident photon, is dependent on photon energy. Meadowcroft *et al* modelled this as,

$$\psi_j = \eta(m_j h\nu + c_j), \quad (1.27)$$

where $h\nu$ is the photon energy and m_j and c_j are linear fit parameters valid for specific energy ranges, j . For the Fuji BAS TR-type IP and for X-rays in the range 0-6.0 keV, $m_j = 0.54(5) \text{ mPSL keV}^{-1}$ and $c_j = 0.020(2) \text{ mPSL}$. The IP absorption efficiency in mPSL per photon is

$$\eta(h\nu, T_i, T_s) = \exp(-n_i \Phi_i(h\nu) T_i) [1 - \exp(-n_s \Phi_s(h\nu) T_s)], \quad (1.28)$$

where n is the layer density, $\Phi(h\nu)$ is the total cross-section of the layer, T the effective layer thickness, s and i correspond to the sensitive (phosphor) and insensitive (mylar) layers of the IP respectively [10]. The first term is neglected in the absence of an insensitive (mylar) layer in TR-type IP. Below 50 keV, the dominant mode for X-ray absorption into the IP is the photo-electric effect, where

$$\Phi_{\text{ph}} \approx 3 \times 10^{12} \frac{Z^4}{(h\nu)^{3.5}} \quad (1.29)$$

and Z is the atomic number [11] and Φ_{ph} is given in units of Barn per atom. At 2.4 keV, that corresponds to a sensitivity of 1.32 mPSL per incident photon.

It is generally inevitable that some time will elapse between laser shot and IP scan. For this experiment 30 minutes was typical, in which time some fading of the IP occurs that must be accounted for. IP fading can be modelled as an attenuation factor,

$$F(t) = A \exp(-t/\tau) + B, \quad (1.30)$$

where t is the time between shot and scan and A , τ and B are found from fits to experimental data. A key aspect of the exponential decay is that the attenuation depends only on the signal at that moment in time and not the initial conditions. This has been shown to be true in experiment [8].

At 20 °C at the ORION facility *Meadowcroft et al* [8] determined that for the Fuji BAS TR-type IP, the optimum fit for the parameters of Equation 1.30 is $A = 0.347(22)$, $B = 0.693(11)$ and $\tau = 35.5(53)$ minutes. Therefore at 30 minutes, $F(t) = 0.84$.

In summary, the number of PSL measured on an IP can be converted to an incident number of photons via

$$N(h\nu) = \frac{\text{PSL}}{F(t)} \frac{10^3}{\psi(h\nu)} = P(h\nu)\text{PSL}. \quad (1.31)$$

1.5.2 OHREX calibration

The Orion High REsolution X-ray spectrometer (OHREX), housed on the ORION laser target chamber outer wall, utilises a spherically bent crystal geometry to spatially focus and spectrally analyse photons from the target chamber [12] with a high signal-to-noise ratio. The measured signal has been absolutely calibrated for a range of energies using a variety of crystals [13]. The OHREX can hold two crystals at a time. At each crystal's spatial focal plane a two-dimensional image is formed, one dimension is spatial, the other spectral. The energy range accessed by a given crystal is determined by the crystal rotation but all OHREX crystals are designed for operation at a nominal central Bragg angle of $\theta_B = 51.3^\circ$ the corresponding wavelength determined from Bragg's Law, $n\lambda = 2d \sin \theta_B$, for the appropriate crystal plane. The range around that central photon energy is determined by the crystal width in the spectral dimension.

MacDonald *et al* determined a quadratic fit for each crystal's dispersion relation to connect position along the image to photon energy [13]. Unfortunately in this experiment, the image lengths varied from those in the previous experiment, a likely consequence of slight defocusing of the optic. Note that the OHREX geometry is designed such that precise focus is not necessary to achieve good results [12].

Crystal	Range, $n = 1$ (eV)	Range, $n = 2$ (eV)
KAP (100)	585-625	1170-1245
Quartz (10̄10)	1830-1950	3660-3900
Quartz (10̄11)	2330-2480	4660-4960

Table 1.2: Photon energy ranges captured by the three lowest energy OHREX crystals when operating at their nominal central Bragg angle of 51.3° or first and second diffraction orders, n .

Instead, a simple linear dispersion relation based on the known maximum and minimum energies accessed by the crystal was applied across the crystal images, a reasonable approximation to the dispersion relation determined by MacDonald *et al* [13] (the quadratic correction is small). The energy ranges for the three lowest energy OHREX crystals are given in table 1.2.

Provided full illumination of the 6 cm × 4 cm crystal, the spatial dimension can be safely integrated over to calculate the measured signal, $M(h\nu)$ in J mm⁻¹ and remove uncertainty from the IP drifting from the ideal focal plane. (In this experiment we assume that the harmonic beam width at the crystal position is larger than the size of the crystal, a reasonable assumption since beam divergence ≈ 10° and the 6 cm x 4 cm crystal sits 2.4 m from the target.). This corresponds to a source spectral intensity incident on the crystal $S(h\nu)$ measured in J keV⁻¹ sr⁻¹ via the spectrometer response, $G(h\nu)$, explicitly,

$$M(h\nu) = S(h\nu)G(h\nu). \quad (1.32)$$

The absolute throughput of the crystals was measured by MacDonald *et al* in a previous ORION experiment and fit parameters for

$$G(h\nu) = A(h\nu)^2 + B(h\nu) + C, \quad (1.33)$$

where $(h\nu)$ is the photon energy measured in eV, determined for both p- and s-polarised incident light and for first and second diffraction orders [13]. The parameters for the lowest few energy crystals are presents in Table 1.3. There is unfortunately no spectrometer response data for the 10̄10 crystal to first order

Crystal	Order	Polarisation	<i>A</i>	<i>B</i>	<i>C</i>
KAP (100)	1	s	1.72×10^{-15}	-4.69×10^{-12}	2.89×10^{-9}
		p	1.40×10^{-14}	-1.74×10^{-11}	5.42×10^{-9}
	2	s	3.64×10^{-16}	-9.64×10^{-13}	6.95×10^{-10}
		p	5.03×10^{-10}	8.09×10^{-13}	5.03×10^{-10}
Quartz (10̄10)	1	s
		p
	2	s	4.50×10^{-15}	-3.40×10^{-11}	6.52×10^{-8}
		p	1.13×10^{-15}	-8.86×10^{-12}	1.73×10^{-8}
Quartz (10̄11)	1	s	1.00×10^{-16}	-1.74×10^{-12}	4.93×10^{-9}
		p	2.78×10^{-15}	-1.41×10^{-11}	1.79×10^{-8}
	2	s	4.70×10^{-16}	-4.50×10^{-12}	1.11×10^{-8}
		p	2.10×10^{-16}	2.11×10^{-12}	5.30×10^{-9}

Table 1.3: Sensitivity fit parameters as a function of photon energy, $h\nu$ in electron-volts ($G(h\nu) = A(h\nu)^2 + B(h\nu) + C$) for the three lowest energy OHREX crystals for p- and s-polarised incident photons and first and second diffraction orders [13]. Note that no data is available for the first order of the quartz (10̄10) crystal.

due to the Si K edge sitting within the energy range and the dramatic effect this has on absorption in its vicinity [14].

The OHREX is equipped with a $50\text{ }\mu\text{m}$ Beryllium filter to protect the crystals. The corresponding signal attenuation can be calculated using X-ray transmission data [15].

1.5.3 Extracting the data

The quartz OHREX crystals 10̄10 and 10̄11 were fielded on the experiment. Crystal images were recorded with BasTR2040 Fuji Image Plate. A typical shot image scanned with the FLA7000 scanner and converted to photostimulated luminescence units (PSLs) is given in Figure 1.7. The average background signal was subtracted. The *x*- and *y*-axes were converted from pixels to mm using the scanner resolution, ($25\text{ }\mu\text{m px}^{-1}$) and then energies using the appropriate dispersion relations. The data was then integrated over *y* to obtain the intensity in units of PSL mm⁻¹ across

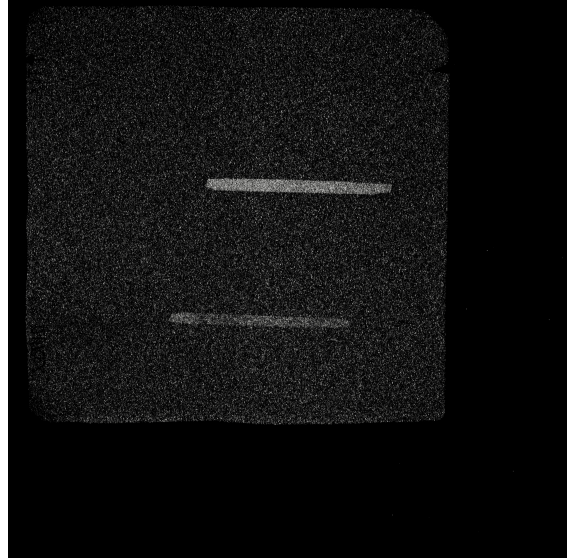


Figure 1.7: Unprocessed shot data from a FLA7000 scanned image plate converted to PSLs. The image plate and two crystal images are clearly visible.

each crystal image. Then the corresponding source signal is

$$S(h\nu)[\text{J keV}^{-1} \text{ sr}^{-1}] = \frac{d\text{PSL}}{dx} \frac{P(h\nu)}{G(h\nu)} h\nu, \quad (1.34)$$

which can then be converted to a measured spectral intensity per harmonic at distance $r = 1$ from the source, ready to be directly compared to the theory,

$$I_n^{\text{meas}}|_{(r=1 \text{ m})} = S(h\nu) \frac{dh\nu(\text{keV})}{dn}. \quad (1.35)$$

No sensitivity data is available for the $10\bar{1}0$ quartz crystal, instead this lower energy crystal was fielded to attempt resolving of the X-ray harmonics. At the experiment planning stage it was unknown if this would be possible. Now that the simulations have been performed, we know that the non-optimal ORION target chamber geometry leads to merging of the harmonics even before the water window at 282 eV. This is consistent with the findings, Figure 1.8 is a typical integrated signal in PSL mm and the corresponding Fourier transform for the quartz ($10\bar{1}0$) crystal image.

Calibration and polarisation

The choice of the spectrometer response function, $G(h\nu)$, is non-trivial. One must firstly be assured that the second order contribution is small relative to the first, true

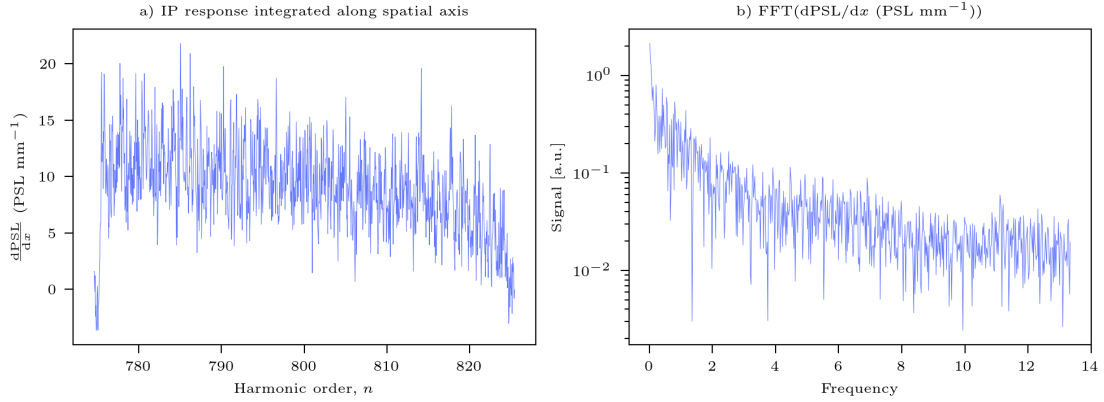


Figure 1.8: Typical (SP1, PMMA) uncalibrated shot data for the quartz (10\bar{1}0) image a) IP spatial axis integrated signal with dispersion axis. b) Fourier transform of a) with no evidence of harmonics.

for this source spectrum. And also think carefully about the anticipated polarisation in the OHREX interaction plane. The OHREX response to p-polarised light is approximately an order of magnitude lower than for s-polarised light. From Figure X we are assured that only the p-polarised (with respect to the target interaction plane) X-rays are specularly reflected to the OHREX. Corresponding polarisation out of the OHREX interaction plane is calculated in the Appendix. The polarisation of the HHG beam relative to the OHREX plane of incidence and reflection is 10.5° out of the plane. Unlike for the RPM interaction, the OHREX crystal reflection is an entirely linear process and it is therefore acceptable to decompose the laser pulse into its constituents, explicitly, the field incident on the crystal is

$$\mathbf{E}_O = \mathbf{E}_{O,s} + \mathbf{E}_{O,p}. \quad (1.36)$$

After interaction with the crystal the field is

$$\mathbf{E}_{\text{detector}} = \alpha_s(h\nu)\mathbf{E}_{O,s} + \alpha_p(h\nu)\mathbf{E}_{O,p}, \quad (1.37)$$

where $\alpha_i(h\nu)$ is the energy dependent ($h\nu$) amplitude sensitivity of the reflection for s- and p-polarised respectively. Since the two polarisations are orthogonal, the intensity is

$$I = \alpha_s^2(h\nu)|\mathbf{E}_{O,s}|^2 + \alpha_p^2(h\nu)|\mathbf{E}_{O,p}|^2. \quad (1.38)$$

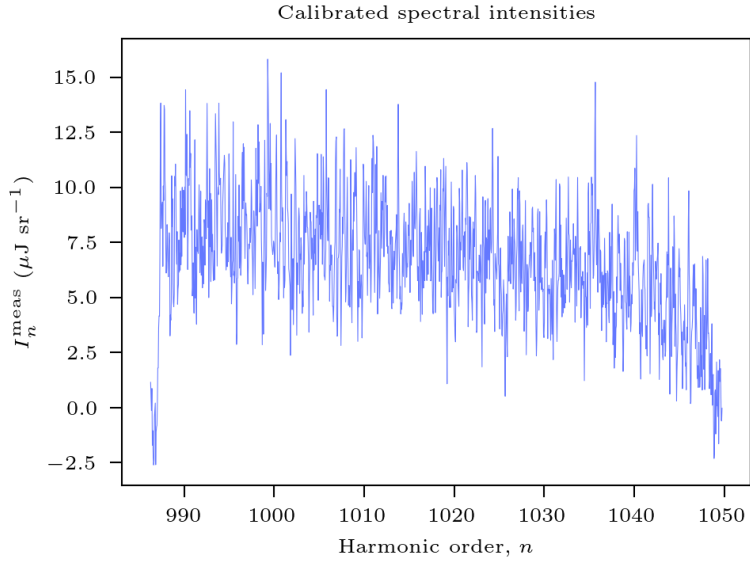


Figure 1.9: Typical (SP1, PMMA) ORION experiment calibrated IP response for the quartz (10̄11) crystal.

Noting that $\alpha_i^2(h\nu)$ are the calibration factors, $G_i(h\nu)$, and that

$$|\mathbf{E}_{\text{O,s}}| = |\mathbf{E}_{\text{O}}| \sin \phi \quad (1.39)$$

and

$$|\mathbf{E}_{\text{O,p}}| = |\mathbf{E}_{\text{O}}| \cos \phi, \quad (1.40)$$

where ϕ is the angle out of the interaction plane,

$$I_{\text{detector}} = (G_s(h\nu) \sin^2 \phi + G_p(h\nu) \cos^2 \phi) |\mathbf{E}_{\text{O}}|^2 = F(h\nu) |\mathbf{E}_{\text{O}}|^2, \quad (1.41)$$

where $F(h\nu) = (G_s(h\nu) \sin^2 \phi + G_p(h\nu) \cos^2 \phi)$ is the energy dependent calibration factor for this OHREX orientation.

Figure 1.9 is a typical calibrated signal from the quartz (10̄11) crystal, ready for comparison to the theoretical prediction.

Shots were also taken through the OHREX port, we had hoped to capture the beam divergence however, the beam was larger than initially expected and we were unable to distinguish much. Mention saturation.

Once done all this analysis, present the data.. Integrated signal across crystal, discuss no harmonics but that is expected and then present the final table and discuss.

Include a table detailing error contributions? Also need to add reflectivity error to the rest.

Discuss mirrored targets and brems emission.

Then go back and do the theory. then sims.

Also in sims look at reconstructing a filtered pulse

Appendices

References

- [1] U. Teubner and P. Gibbon. “High-Order Harmonics from Laser-Irradiated Plasma Surfaces”. In: *Reviews of Modern Physics* 81.2 (Apr. 3, 2009), pp. 445–479.
- [2] S C Wilks et al. *Absorption of Ultra-Intense Laser Pulses*. 1992.
- [3] Henri Vincenti. “Achieving Extreme Light Intensities Using Optically Curved Relativistic Plasma Mirrors”. In: *Physical Review Letters* 123.10 (Sept. 3, 2019). pmid: 31573299.
- [4] H. Vincenti et al. “Optical Properties of Relativistic Plasma Mirrors”. In: *Nature Communications* 5 (Mar. 11, 2014), p. 3403. pmid: 24614748.
- [5] A. P.L. Robinson et al. “Relativistically Correct Hole-Boring and Ion Acceleration by Circularly Polarized Laser Pulses”. In: *Plasma Physics and Controlled Fusion* 51.2 (2009).
- [6] A. P.L. Robinson, D. H. Kwon, and K. Lancaster. “Hole-Boring Radiation Pressure Acceleration with Two Ion Species”. In: *Plasma Physics and Controlled Fusion* 51.9 (2009).
- [7] Matthew R. Edwards and Julia M. Mikhailova. “The X-Ray Emission Effectiveness of Plasma Mirrors: Reexamining Power-Law Scaling for Relativistic High-Order Harmonic Generation”. In: *Scientific Reports* 10.1 (Dec. 1, 2020), p. 5154. pmid: 32198482.
- [8] A. L. Meadowcroft, C. D. Bentley, and E. N. Stott. “Evaluation of the Sensitivity and Fading Characteristics of an Image Plate System for X-Ray Diagnostics”. In: *Review of Scientific Instruments* 79.11 (Nov. 11, 2008), p. 113102.
- [9] D. O. Golovin et al. “Calibration of Imaging Plates Sensitivity to High Energy Photons and Ions for Laser-Plasma Interaction Sources”. In: *Journal of Instrumentation* 16.02 (Feb. 2021), T02005.
- [10] N. Izumi et al. “Application of Imaging Plates to X-Ray Imaging and Spectroscopy in Laser Plasma Experiments (Invited)”. In: *Review of Scientific Instruments* 77.10 (Oct. 23, 2006), 10E325.
- [11] Krzysztof W Fornalski. “Simple Empirical Correction Functions to Cross Sections of the Photoelectric Effect, Compton Scattering, Pair and Triplet Production for Carbon Radiation Shields for Intermediate and High Photon Energies”. In: *Journal of Physics Communications* 2.3 (Mar. 22, 2018), p. 035038.
- [12] P. Beiersdorfer et al. “Lineshape Spectroscopy with a Very High Resolution, Very High Signal-to-Noise Crystal Spectrometer”. In: *Review of Scientific Instruments* 87.6 (June 1, 2016).

- [13] M. J. MacDonald et al. “Absolute Throughput Calibration of Multiple Spherical Crystals for the Orion High-REsolution X-ray Spectrometer (OHREX)”. In: *Review of Scientific Instruments* 92.2 (Feb. 1, 2021). pmid: 33648146.
- [14] N. Hell et al. “Calibration of the OHREX High-Resolution Imaging Crystal Spectrometer at the Livermore Electron Beam Ion Traps”. In: *Review of Scientific Instruments* 87.11 (Nov. 1, 2016), p. 11D604.
- [15] B. L. Henke, E. M. Gullikson, and J. C. Davis. “X-Ray Interactions: Photoabsorption, Scattering, Transmission, and Reflection at $E = 50\text{-}30,000 \text{ eV}$, $Z = 1\text{-}92$ ”. In: *Atomic Data and Nuclear Data Tables* 54.2 (July 1, 1993), pp. 181–342.